Supplemental Information for
Loss induced delocalization of topological boundary modes

Yugan Tang[1†], Jien Wu[2†], Pengtao Lai[1], Yejian Hu[3], Hui Liu[1], Weiyin Deng[3*], Hua Cheng[1*], Zhengyou Liu[3,4*], and Shuqi Chen[1,5,6*]

[1]The Key Laboratory of Weak Light Nonlinear Photonics, Ministry of Education, School of Physics and TEDA Institute of Applied Physics, Nankai University, Tianjin 300071, China
[2]School of Physics and Electronic Science, Changsha University of Science and Technology, Changsha 410114, China
[3]Key Laboratory of Artificial Micro- and Nanostructures of Ministry of Education and School of Physics and Technology, Wuhan University, Wuhan 430072, China
[4]Institute for Advanced Studies, Wuhan University, Wuhan 430072, China
[5]School of Materials Science and Engineering, Smart Sensing Interdisciplinary Science Center, Nankai University, Tianjin 300350, China
[6]The Collaborative Innovation Center of Extreme Optics, Shanxi University, Taiyuan, Shanxi 030006, China

†These authors contributed equally to this work.
*Corresponding author.
Emails: dengwy@whu.edu.cn; hcheng@nankai.edu.cn; zyliu@whu.edu.cn; schen@nankai.edu.cn

Table of Contents

1. Topological properties of the 1D bilayer non-Hermitian SSH chain.

The Hamiltonian in Eq. (1) of main text is separated into two independent blocks with energy eigenvalues of $E_{\uparrow(\downarrow)} = \pm\sqrt{(t_1\cos k + i\gamma)^2 + (t_1\sin k + (-)t_0)^2}$ where the corresponding eigenstates can be expressed as $\psi_{\uparrow(\downarrow)} = \frac{1}{\sqrt{2}}[\psi_1 + (-)i\psi_3, \psi_2 + (-)i\psi_4]^T$. Due to the introduction of loss, the topological characteristics of the system cannot be described by the bulk Hamiltonian of PBC. We employ the generalized Brillouin zone (GBZ) to solve this problem [1]. Taking spin down model as an example, where the real-space bulk eigen-equations under open boundary condition (OBC) are rewritten as

$$E_{1\downarrow}B_{\downarrow,l} = t_bA_{\downarrow,l} + t_1A_{\downarrow,l+1},\ E_{1\downarrow}A_{\downarrow,l} = t_1B_{\downarrow,l-1} + t_aB_{\downarrow,l}, \tag{S1}$$

where $t_a = i(\gamma - t_0)$ and $t_b = i(\gamma + t_0)$, $A_{\downarrow,l}$ and $B_{\downarrow,l}$ represent the wavefunction components on the l-th site A and site B, respectively. For the definition of $A_{\downarrow,l} = \beta^{l-1}A_{\downarrow,1}$ and $B_{\downarrow,l} = \beta^{l-1}B_{\downarrow,1}$, we have

$$E_{1\downarrow}^2 = (t_b + t_1\beta)(t_a + t_1\beta^{-1}), \tag{S2}$$

which has two solutions with

$$\beta_{1,2} = \left[E_{1\downarrow}^2 - t_1^2 - t_at_b \pm \sqrt{-4t_1^2t_at_b + \left(t_1^2 + t_at_b - E_{1\downarrow}^2\right)}\right]/2t_1t_a.$$

Then, we obtain $\beta_1\beta_2 = t_b/t_a$. Considering a long chain, which requires $|\beta_1| = |\beta_2|$ for the bulk eigenstates, leading to

$$|\beta_{1,2}| = r_\downarrow = \sqrt{\left|\frac{t_b}{t_a}\right|}. \tag{S3}$$

Then, the GBZ of bulk modes for spin down is described as $\beta_\downarrow = \sqrt{\left|\frac{t_b}{t_a}\right|}\,e^{ik}$. In a similar way, the GBZ of bulk modes for spin up is obtained as $\beta_\uparrow = \sqrt{\left|\frac{t_a}{t_b}\right|}\,e^{ik}$. A point in the GBZ corresponds to an OBC eigenstate, whose wavefunction at l-th sublattice site satisfies $\psi_l \propto \beta^l$. Compared with the unit circle of Brillouin zone (BZ), when $\gamma = -t_0 \pm |t_1|$ as the critical γ_c, $|\beta_\uparrow| < 1$ (left-localized) and $|\beta_\downarrow| > 1$ (right-localized) indicate that the OBC bulk modes become spin polarized non-Hermitian skin effects (NHSEs), as shown in Figs. S1a and S1b. According to the different time-reversal symmetry, the reciprocal bilayer system is characterized by spin-dependent spectral

topology, which differ from the spinless topology in non-reciprocal systems. The spectral topology can be classified by employing the current functional [2], i.e., $J_{\boldsymbol{\alpha}}[n] = \sum_i \oint_{\mathrm{BZ}} dk^d n(E_i, E_i^*) \nabla_{\boldsymbol{\alpha}} E_i(k)$, where $n(E_i, E_i^*)$ represents the distribution function when the system reaches to a steady state, i indicates the energy band index, and $\nabla_{\boldsymbol{\alpha}}$ is the directional derivative along direction $\boldsymbol{\alpha}$ in d-dimension. The spin polarized NHSEs originate from the spin-dependent spectral topology related to zero current functionals $J = 0$, which distinguishes from the spinless spectral topology in non-reciprocal model with non-zero current functionals $J \neq 0$.

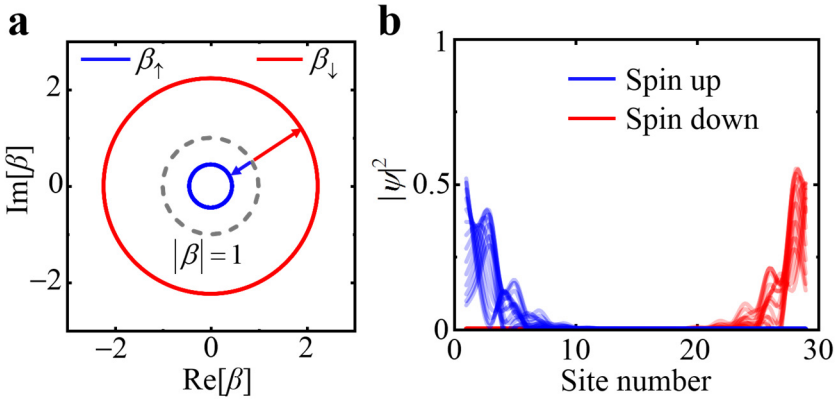

Figure S1 | Loss induced spin polarized NHSEs. a GBZs of this model. **b** Wavefunction intensities of all the bulk modes for two spins at $\gamma = \gamma_c$. The parameters are chosen as $t_0 = 0.6$, $t_1 = -1$ with $\gamma_c = 0.4$.

The non-Bloch Hamiltonian can be derived from $H_{1\uparrow(\downarrow)}$ in the main text and expressed as

$$H_{1\uparrow}(\beta_\uparrow) = (t_a + t_1\beta_\uparrow)\sigma_- + (t_b + t_1\beta_\uparrow^{-1})\sigma_+,$$
$$H_{1\downarrow}(\beta_\downarrow) = (t_b + t_1\beta_\downarrow)\sigma_- + (t_a + t_1\beta_\downarrow^{-1})\sigma_+, \quad \text{(S4)}$$

where $\sigma_\pm = (\sigma_x \pm i\sigma_y)/2$. The corresponding energy eigenvalues can be written as

$$E_{1\uparrow}^2(\beta_\uparrow) = t_1^2 + t_a t_b + t_1(t_b\beta_\uparrow + t_a\beta_\uparrow^{-1}),$$
$$E_{1\downarrow}^2(\beta_\downarrow) = t_1^2 + t_a t_b + t_1(t_a\beta_\downarrow + t_b\beta_\downarrow^{-1}), \quad \text{(S5)}$$

which indicating that OBC energy gap closes at $\gamma = \pm\sqrt{t_1^2 + t_0^2}$ and is different from the closure point of periodic boundary condition (PBC) spectrum with $\gamma = \pm t_0 \pm |t_1|$. The closure point of OBC spectrum is same for two spins with $|E_{1\uparrow}(\beta_\uparrow)| = |E_{1\downarrow}(\beta_\downarrow)| =$

0. In another way, based on Eq. (S5), we have

$$\beta_1^{E_{1\downarrow}=0} = -\frac{t_b}{t_1},\ \beta_2^{E_{1\downarrow}=0} = -\frac{t_1}{t_a}, \tag{S6}$$

which describe the wavefunction decays of the left and right end modes for spin down, respectively. Owing to the zero energy $E_{1\downarrow} = 0$, the wavefunction components of end modes on site B are zero with $B_\downarrow = 0$. In addition, the Bloch phase factors of the end modes for spin up can be expresses as

$$\beta_1^{E_{1\uparrow}=0} = -\frac{t_a}{t_1},\ \beta_2^{E_{1\uparrow}=0} = -\frac{t_1}{t_b}. \tag{S7}$$

For simplified, we cut off two sites at right end of the duplex chain and leave only end modes at left. The amplitudes of the left end modes' wavefunctions at l-th site A can be derived as $|A_{\uparrow,l}| = c_\uparrow|\epsilon_{A,\uparrow}|^{l-1}$ and $|A_{\downarrow,l}| = c_\downarrow|\epsilon_{A,\downarrow}|^{l-1}$ for spin up and spin down, respectively. The wavefunction decay ratios are $\epsilon_{A,\uparrow} = \beta_1^{E_{1\uparrow}=0} = -i\frac{\gamma - t_0}{t_1}$ and $\epsilon_{A,\downarrow} = \beta_1^{E_{1\downarrow}=0} = -i\frac{\gamma + t_0}{t_1}$, $c_\uparrow$ and $c_\downarrow$ are the normalized coefficients. For spin down, when $\gamma < \gamma_c$ there is $|\epsilon_{A,\downarrow}| < 1$, the end mode is localized at the left end; when $\gamma = \gamma_c$, there is $|\epsilon_{A,\downarrow}| = 1$, resulting in a TDM instead of a localized mode; when $\gamma > \gamma_c$ and then $|\epsilon_{A,\downarrow}| > 1$, the end mode is more delocalized at the right end. The wavefunction decay ratios of the left end modes for two spins are displayed in Fig. S2a. Therefore, loss counteracts the localization of topological boundary mode (TBM) by changing its wavefunction decay ratio. The corresponding wavefunction intensities for two spins are shown in Fig. S2b to illustrate this.

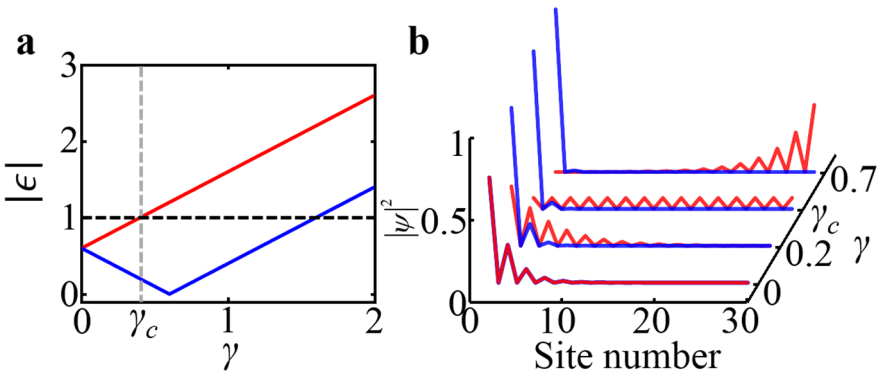

Figure S2 | Loss induced spin polarized delocalization of end modes. a Magnitudes of the left end modes' wavefunction decay ratios for two spins as a function of γ. **b**

Wavefunction intensities of the end modes for two spins as a function of γ. The red and blue lines represent the results for spin down and spin up, respectively. The parameters are chosen as $t_0 = 0.6,\ t_1 = -1$ with $\gamma_c = 0.4$.

To investigate the localization property and the topological property of end modes, we employ both Bloch winding number defined in BZ and non-Bloch winding number defined in GBZ. Although the bulk-boundary correspondence is breakdown, the Bloch winding number defined in BZ can still be employed to describe the localization property of end modes in 1D [3-5]. Based on Eq. (S4), the Bloch and non-Bloch Hamiltonians with chiral symmetry have the same form as $H(\beta) = \begin{pmatrix} 0 & H_{ab}(\beta) \\ H_{ba}(\beta) & 0 \end{pmatrix}$, but $\beta = \beta_{\mathrm{BZ}} = e^{ik}$ and $\beta = \beta_{\mathrm{GBZ}} = e^{ik'}$, respectively. The Bloch winding number is defined as

$$W_{\mathrm{BZ}} = \frac{1}{2\pi}\oint_{\mathrm{BZ}} \arg\frac{H_{ab}(\beta_{\mathrm{BZ}})}{H_{ba}(\beta_{\mathrm{BZ}})}\, d\beta_{\mathrm{BZ}}, \tag{S8}$$

while the non-Bloch one is expressed as

$$W_{\mathrm{GBZ}} = \frac{1}{2\pi}\oint_{\mathrm{GBZ}} \arg\frac{H_{ab}(\beta_{\mathrm{GBZ}})}{H_{ba}(\beta_{\mathrm{GBZ}})}\, d\beta_{\mathrm{GBZ}}. \tag{S9}$$

Evidently, the ratio of two Laurent polynomials $M(\beta) = \frac{H_{ab}(\beta)}{H_{ba}(\beta)}$ defines a meromorphic function on the complex plane, while either $H_{ab}(\beta) = 0$ or $H_{ba}(\beta) = 0$ will make $M(\beta)$ become zero or infinite, indicating the zero or pole points. These winding numbers have physical meanings and can be understood by the difference between pole and zero points in BZ and GBZ, i.e., $W_{\mathrm{BZ}} = Z_{\mathrm{BZ}} - P_{\mathrm{BZ}}$ and $W_{\mathrm{GBZ}} = Z_{\mathrm{GBZ}} - P_{\mathrm{GBZ}}$, where the total number Z (P) denotes the total number of zero (pole) points inside the BZ or GBZ [6-8]. Moreover, owing to the winding numbers derived from the zero-pole method are identical to twice the results calculated by the "Q matrix" [1], we multiplied the topological invariants by 1/2. The corresponding topological phases of the spin down model have been calculated as a function of γ and shown in Fig. 1b of main text, which is the same for spin up. It can be found that the topological phase transition points are at $\gamma = \pm\sqrt{t_1^2 + t_0^2}$ (non-Bloch winding number) and $\gamma = \pm t_0 \pm |t_1|$ (Bloch winding number), which are the same with the closure points of

OBC and PBC spectra, respectively.

While the critical parameter γ_c can be understood as the topological transition point of Bloch winding number. Before and after the transition point, the localization direction of the end mode will change; at the transition point, the end mode naturally becomes delocalized. The physical meaning of the transition point γ_c can be understood by the change of zero and pole points within BZ. As an intuitive illustration, the $\beta^{E=0}$ of end mode is exactly a zero (pole) point for making $H_{ab}(\beta) = 0$ or $H_{ba}(\beta) = 0$, while the $\beta = 0$ is always a pole point for making β^{-1} infinite. In the spin down model, the $\beta_1^{E_{1\downarrow}=0}$ of left end mode and $\beta = 0$ are the only two pole points in the GBZ before OBC gap close. Therefore, when the $\beta_1^{E_{1\downarrow}=0}$ is inside the BZ, there are $W_{\mathrm{GBZ}} = 1$ and $W_{BZ} = 1$; when $\beta_1^{E_{1\downarrow}=0}$ intersects with BZ, i.e., $\gamma = \gamma_c$, the W_{BZ} is thus changed to $W_{\mathrm{BZ}} = 1/2$ while the $W_{GBZ} = 1$ keeps unchanged; when $\beta_1^{E_{1\downarrow}=0}$ intersects with GBZ, the W_{GBZ} is changed to $W_{\mathrm{GBZ}} = 0$, indicating the disappearance of end mode. The $\arg(M(\beta))$ at $\gamma = \gamma_c$ displayed in Fig. S3 clearly shows the change of end mode's localization property. At this time, $\beta_1^{E_{1\downarrow}=0}$ and a point of β_{BZ} possess the same value, which leads to the same eigenvalues in spectra based on Eq. (S5).

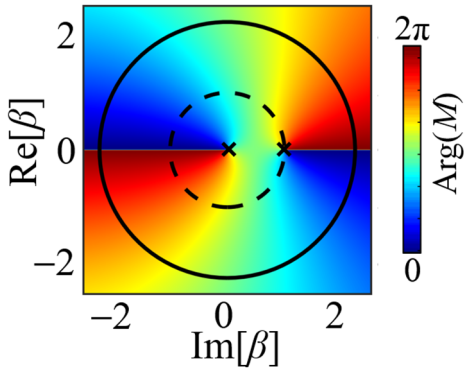

Figure S3 | Physical meaning of the transition point γ_c. β-plane colored by $\arg(M(\beta))$ at $\gamma = \gamma_c$ with GBZ in black line, BZ in black dotted line, and poles of $M(\beta)$ as $\times$ marker. The $\beta_1^{E_{1\downarrow}=0} = i$ is a pole of $M(\beta)$ and intersects with BZ, indicating the change of Bloch winding number.

2. Discussion in delocalization of the TBMs under the condition of end modes at two ends.

In a similar way of main text, we take spin down model as an example and keep it intact with 30 sites ($N = 15$). There are two nontrivial end modes localized at left and right end of the chain in Hermitian cases, respectively, as shown in Figs. S4a and S4b. The parameters are chosen as $t_0 = 0.6$ and $t_1 = -1$. Since these two end modes are degenerate, we add an on-site perturbation $m = 0.001$ to decouple them with

$$H_{\downarrow}(k) = \begin{pmatrix} m & t_a + t_1 e^{-ik} \\ t_b + t_1 e^{ik} & -m \end{pmatrix}. \tag{S10}$$

Based on Eq. (S1), we can obtain the magnitude ratios of the two end modes with $\epsilon_{A,\downarrow} = \left|\frac{t_b}{t_1}\right|$ and $\epsilon_{B,\downarrow} = \left|\frac{B_{\downarrow,l-1}}{B_{\downarrow,l}}\right| = \left|\frac{t_a}{t_1}\right|$, respectively. When we set $\gamma = \gamma_c$ to delocalize the left end mode with $\epsilon_{A,\downarrow} = 1$, the right end mode is more bound due to $\epsilon_{B,\downarrow} < 1$. It seems that the left end mode will become a flat TDM and the right one will form a bound mode. However, owing to the chiral symmetry guarantees zero energy for the end modes, the left end mode that originally occupies site A will be finally localized at right end and distributes in site B to meet the open-boundary conditions, as shown in Figs. S4c and S4d. To explain this, let us write its real-space eigen-equations at boundaries with $E_{1\downarrow}A_{\downarrow,1} = t_a B_{\downarrow,1}$ at left end and $E_{1\downarrow}B_{\downarrow,N} = t_b A_{\downarrow,N}$ at right end. The chiral symmetry imposes $E_{1\downarrow} = 0$ to end mode, which necessitates $A_{\downarrow,N} = 0$ at right end. While the loss induced delocalization forces the left end mode to become TDM with $\epsilon_{A,\downarrow} = 1$, resulting in zero wavefunctions on all site A. The left end mode finally distributes in site B and bound to the right end. Hence, we cut off two sites at the right end of the dual-layered chain to avoid this. In another way, the delocalization of TBMs under the condition of end modes at two ends can be realized by breaking the chiral symmetry.

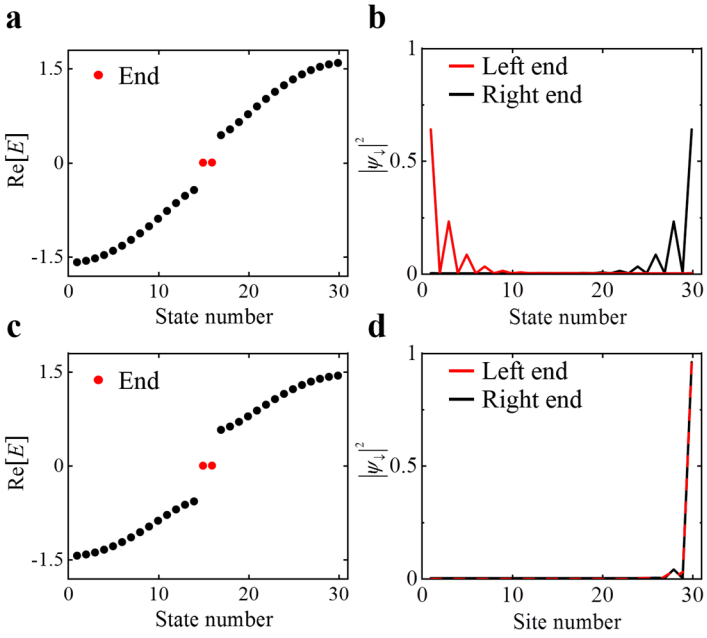

Figure S4 | Condition of TBMs at two ends for spin down chain. a, c OBC real energy spectrum in Hermitian cases with $\gamma = 0$ and non-Hermitian cases with $\gamma = \gamma_c$, respectively. **b, d** Corresponding wavefunction intensity distributions of the two end modes.

3. Significance of the reciprocal theory and passive experiment.

Among almost all previous studies, it is widely accepted that the loss can cause the localization of eigenstate at boundary, i.e., the generalized reciprocal skin effect. Nevertheless, to the best of our knowledge, there is no theory and experiment to discuss how to delocalize the originally localized states by employing loss. Our work utilizing loss to delocalize the TBMs is significant. As shown in Fig. S5a, the reciprocal bilayer structure, incorporating pseudospin degree of freedom and loss, exhibits powerful performance when compared with a single-layer structure under identical loss parameters. By employing solely loss, the in-gap TBM under OBC can coincide with the PBC spectrum at $\gamma = \gamma_c$, forming the Bloch point, as shown in the middle of Fig. S5a, thereby delocalizing the TBM into a TDM. As a result, our study offers a fundamentally distinct insight for understanding of non-Hermitian loss, and establishes a distinct paradigm for manipulating TBMs via a reciprocal way. Meanwhile, the proposed reciprocal strategy with loss employs simple passive components, which

undoubtedly contribute to making the non-Hermitian systems remain stable while maintaining compact size. For instance, the non-Hermitian loss in the circuit only requires a single resistor, as shown in the right side of Fig. S5a.

It is essentially different from the non-reciprocal methods, which are widely used in realizing the non-Hermitian topological effects. For instance, the conventional 1D non-reciprocal SSH model for realizing TDMs is shown in Fig. S5b, which is identical to that reported in Ref. [9]. By tuning the strength of non-reciprocal interaction, the in-gap TBM under OBC can coincide with PBC spectrum, forming the TDM. However, even in circuit implementations, a single non-reciprocal hopping usually requires a complicated impedance converter circuit with external DC power supplies. The typical impedance converter circuit of Refs. [10, 11] is illustrated in the right side of Fig. S5b. Such non-reciprocal interactions entail two widely recognized drawbacks in experiment: first, they predominantly rely on active devices or bulky configurations that necessitate external intervention, significantly increasing system bulk and impeding device miniaturization and development in high-dimensional systems; second, once the number of active components increases or the non-reciprocal hopping strength surpasses a certain magnitude, the system may become unstable accompanied by self-excited oscillations, which limit the number of sites and complicate the validation of models in high-dimension. Thus, the presented reciprocal theory and experiment bring distinct insights to the study of states in non-Hermitian physics, and are more readily extensible and implementable in research and experiments involving high-dimensional or other systems.

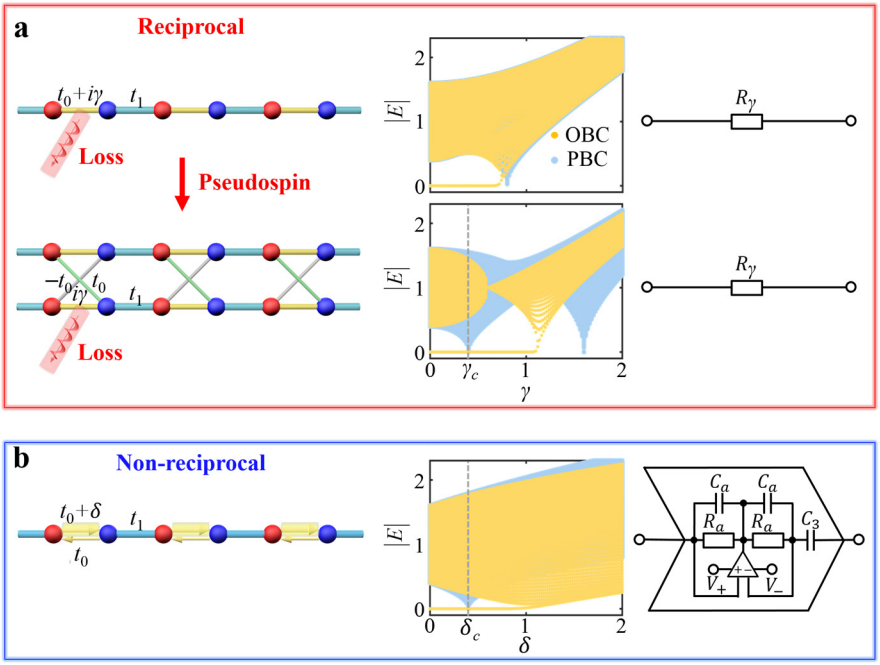

Figure S5 | Significance of the proposed reciprocal theory and passive experiment. **a** Comparison between single-layer model with loss and bilayer model with pseudospin degree of freedom and loss. The red and blue balls conceptually indicate the corresponding sublattices. The yellow and light blue sticks are intracell and intercell hoppings, respectively, where the red vortex represents loss. The grey and green sticks represent the positive and negative hopping, respectively. The Bloch point is formed at $\gamma = \gamma_c$ for bilayer model. The reciprocal hopping with loss is realized by utilizing only a resistor. **b** Conventional 1D non-reciprocal SSH model. The non-reciprocal hoppings are indicated by yellow arrows. The OBC and PBC spectra are plotted in the middle. The typical non-reciprocal hopping is realized by employing the impedance converter circuit. The parameters are $t_0 = 0.6$, $t_1 = -1$ with $\gamma_c = 0.4$ and $\delta_c = 0.4$.

4. 1D passive electric circuit corresponding to the bilayer non-Hermitian chain.

Next, we focus on the design of the 1D passive circuit. According to the circuit model shown in Fig. 2a of main text, the relation between the input current and voltage of each node can be written via Kirchhoff's law as

$$I_{1,l} = \left(\frac{1}{i\omega L_0} + i\omega C_1\right)V_{1,l} + \frac{1}{R_1}\left(V_{1,l} - V_{2,l}\right) + i\omega C_2\left(V_{1,l} - V_{2,l-1}\right)$$
$$+i\omega C_0\left(V_{1,l} - V_{4,l}\right),$$

$$I_{2,l}=\left(\frac{1}{i\omega L_0}+i\omega C_1+i\omega 2C_0\right)V_{2,l}+\frac{1}{R_1}\left(V_{2,l}-V_{1,l}\right)+i\omega C_2\left(V_{2,l}-V_{1,l+1}\right)$$
$$+\frac{1}{i\omega L_0}\left(V_{2,l}-V_{3,l}\right),$$
$$I_{3,l}=\left(\frac{1}{i\omega L_0}+i\omega C_1+i\omega 2C_0\right)V_{3,l}+\frac{1}{R_1}\left(V_{3,l}-V_{4,l}\right)+i\omega C_2\left(V_{3,l}-V_{4,l-1}\right)$$
$$+\frac{1}{i\omega L_0}\left(V_{3,l}-V_{2,l}\right),$$
$$I_{4,l}=\left(\frac{1}{i\omega L_0}+i\omega C_1\right)V_{4,l}+\frac{1}{R_1}\left(V_{4,l}-V_{3,l}\right)+i\omega C_2\left(V_{4,l}-V_{3,l+1}\right)$$
$$+i\omega C_0\left(V_{4,l}-V_{1,l}\right), \tag{S11}$$

where $I_{\alpha,l}$ and $V_{\alpha,l}$ represent the input current and voltage against ground at node α in the l-th unit cell. By applying Bloch's theorem, we obtain

$$[I_{1,l},I_{2,l},I_{3,l},I_{4,l}]^T=J_1(k)[V_{1,l},V_{2,l},V_{3,l},V_{4,l}]^T. \tag{S12}$$

The circuit Laplacian can be deduced with

$$J_1(k)=i\omega[H_1(k)+E_1], \tag{S13}$$

where

$$H_1(k)=\begin{pmatrix} 0 & -C_2\mathrm{e}^{-ik}+\frac{i}{\omega R_1} & 0 & -C_0 \\ -C_2\mathrm{e}^{ik}+\frac{i}{\omega R_1} & 0 & \frac{1}{\omega^2 L_0} & 0 \\ 0 & \frac{1}{\omega^2 L_0} & 0 & -C_2\mathrm{e}^{-ik}+\frac{i}{\omega R_1} \\ -C_0 & 0 & -C_2\mathrm{e}^{ik}+\frac{i}{\omega R_1} & 0 \end{pmatrix},$$

diagonal matrix $E_1=\mathrm{diag}(A_1,A_2,A_2,A_1)$ with $A_1=C_0+C_1+C_2-\frac{1}{\omega^2 L_0}-\frac{i}{\omega R_1}$ and $A_2=2C_0+C_1+C_2-2\frac{1}{\omega^2 L_0}-\frac{i}{\omega R_1}$. The $H_1(k)$ in circuit is the same with it in lattice model through the correspondences in the main text. Owing to the equal interlayer hoppings require $f=\frac{1}{2\pi\sqrt{L_0C_0}}$, the diagonal components are also the same at this frequency with $A_1=A_2$. Therefore, the circuit Laplacian can still be separated into two blocks with $J_1'(k)=\begin{pmatrix} J_{1\uparrow}(k) & 0 \\ 0 & J_{1\downarrow}(k)\end{pmatrix}$ via the unitary transformation of $J_1'(k)=T_1J_1(k)T_1^{-1}$ at f_0. The $J_{1\uparrow\downarrow}(k)$ at f_0 can be written as

$$J_{1\uparrow}(k)=i\omega_0\begin{pmatrix} A_1 & -C_2\mathrm{e}^{-ik}+i(\frac{1}{\omega R_1}+\frac{C_0}{2}+\frac{1}{2\omega^2 L_0}) \\ -C_2\mathrm{e}^{ik}+i(\frac{1}{\omega R_1}-\frac{C_0}{2}-\frac{1}{2\omega^2 L_0}) & A_1 \end{pmatrix},$$

$$J_{1\downarrow}(k)=i\omega_0\begin{pmatrix} A_1 & -C_2\mathrm{e}^{-ik}+i(\frac{1}{\omega R_1}-\frac{C_0}{2}-\frac{1}{2\omega^2 L_0}) \\ -C_2\mathrm{e}^{ik}+i(\frac{1}{\omega R_1}+\frac{C_0}{2}+\frac{1}{2\omega^2 L_0}) & A_1 \end{pmatrix}. \tag{S14}$$

Obviously, forming a TDM requires $R_1=\frac{2\pi}{f_0(-C_0\mp C_2)}$ as the critical R_{1c} to reach $\gamma=\gamma_c$ for spin down model. In our design, $R_1=6.65\ \Omega$ at $f_0=161.8$ kHz.

5. Details of 2D bilayer non-Hermitian lattice.

The Hamiltonian of the bilayer kagome lattice shown in Fig. 3a of main text can be written as

$$H_2(\boldsymbol{k})=\begin{pmatrix} 0 & i\gamma+h_{12} & i\gamma+h_{13} & 0 & -t_0 & -t_0 \\ i\gamma+h_{12}^* & 0 & h_{23} & t_0 & 0 & 0 \\ i\gamma+h_{13}^* & h_{23}^* & 0 & t_0 & 0 & 0 \\ 0 & t_0 & t_0 & 0 & i\gamma+h_{12} & i\gamma+h_{13} \\ -t_0 & 0 & 0 & i\gamma+h_{12}^* & 0 & h_{23} \\ -t_0 & 0 & 0 & i\gamma+h_{13}^* & h_{23}^* & 0 \end{pmatrix}, \tag{S15}$$

where $h_{12}=t_1e^{-ik_x}$, $h_{13}=t_1e^{-i(k_x+\sqrt{3}k_y)/2}$ and $h_{23}=t_1e^{-i(-k_x+\sqrt{3}k_y)/2}$. Its basis is based on $\psi=[\psi_{1\mathrm{up}},\psi_{2\mathrm{up}},\psi_{3\mathrm{up}},\psi_{1\mathrm{down}},\psi_{2\mathrm{down}},\psi_{3\mathrm{down}}]^T$. Similarly, it can also be decoupled into into two spin parts with $H_2'(\boldsymbol{k})=\begin{pmatrix} H_{2\uparrow}(\boldsymbol{k}) & 0 \\ 0 & H_{2\downarrow}(\boldsymbol{k}) \end{pmatrix}$ via the unitary transform $H_2'(\boldsymbol{k})=T_2H_2(\boldsymbol{k})T_2^{-1}$, where the transform matrix can be expressed as

$$T_2=\frac{1}{\sqrt{2}}I_3\otimes\begin{pmatrix} 1 & i \\ 1 & -i \end{pmatrix}. \tag{S16}$$

The corresponding spin polarized eigenstates can be obviously obtained as $\psi_{\uparrow(\downarrow)}=\frac{1}{\sqrt{2}}[\psi_{1\mathrm{up}}+(-)i\psi_{1\mathrm{down}},\psi_{2\mathrm{up}}+(-)i\psi_{2\mathrm{down}},\psi_{3\mathrm{up}}+(-)i\psi_{3\mathrm{down}}]^T$.

The second-order corner modes can be described by the non-Hermitian bulk polarizations. In the 2D system, the non-Hermitian bulk polarization is defined as $P_i=-\frac{1}{S}\int_{BZ}\mathrm{Tr}[A_i]\,d^2k$, where $i=x,y$, $A_i(k)=i\langle u_{m,k}^L|\partial_{k_i}|u_{n,k}^R\rangle$ is the Berry connection of the lowest band, $\langle u_{m,k}^L|$ and $|u_{n,k}^R\rangle$ represent the m-th left and n-th right eigenvectors, respectively. It need to be mentioned that the left eigenvectors are

obtained via $H^{\dagger}(k)|u^{L}_{m,k}\rangle = E^{*}_{m}|u^{L}_{m,k}\rangle$ to satisfy the biorthogonal relations for non-Hermitian case [12]. The bulk polarization can be subsequently calculated via Wilson loop approach with $P_y = \frac{1}{2\pi}\int_{k_y} dv_2$, where v_2 is the Berry phase along the closed loop k_x at fixed k_y, while P_x can be obtained via the similar way. The bulk polarization of 2D spin down model is calculated along the k_x and k_y directions of BZ (Fig. S6a). The topological phase diagram is draw in Fig. S6b. It is also the same for spin up. The nontrivial phase with $P_y = -1/2\sqrt{3}$ is described by the green color, indicating the Wannier centers located at the centers of the downward-pointing triangles, marked by red stars in Fig. S6b. The trivial phase with $P_y = 0$ represented by blue color indicates the Wannier centers located at the centers of the upward-pointing triangles. The Wannier band v_2 calculated along the closed loop k_x for critical parameters (marked by blue stars in Fig. S6b) is displayed in Fig. S6c.

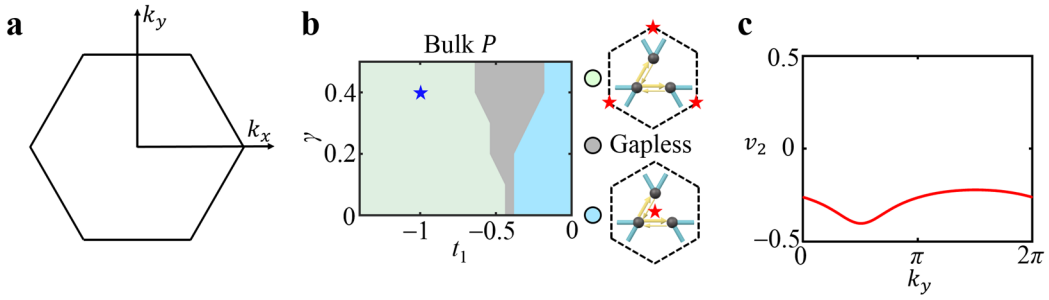

Figure S6 | Topological phases of the 2D and 3D spin down models. a First BZ of the kagome lattice. **b** Topological phase diagram of 2D model with $t_0 = 0.6$. The red stars indicate the location of Wannier centers. The green, gray and blue colors indicate the nontrivial phase, gapless and trivial phase, respectively. **c** Wannier band v_2 vary with k_x.

6. 2D passive electric circuit's design and property.

Similar to the 1D case, we can derive the 2D circuit Laplacian by applying Kirchhoff's law with $J_2(\boldsymbol{k}) = i\omega[H_2(\boldsymbol{k}) + E_2]$, where $H_2(\boldsymbol{k})$ is the same with Eq. (S15) via the correspondences in the main text. To simplify the schematic, the circuit elements grounded at each node are not exhibited in Fig. 4b of main text. Each node is

grounded through an inductance L_0 and a capacitance C_1. Besides, to make the diagonal components consistent at the critical frequency f_0, nodes 2 and 3 are both grounded a R_1 and three C_0; node 4 is grounded four C_0; nodes 5 and 6 are both grounded a R_1 and a C_0. The diagonal matrix can be expressed as $E_2 = \mathrm{diag}(B_1, B_2, B_2, B_3, B_1, B_1)$, where $B_1 = 2C_0 + C_1 + 2C_2 - \frac{1}{\omega^2 L_0} - 2\frac{i}{\omega R_1}$, $B_2 = 3C_0 + C_1 + 2C_2 - 2\frac{1}{\omega^2 L_0} - 2\frac{i}{\omega R_1}$, $B_3 = 4C_0 + C_1 + 2C_2 - 3\frac{1}{\omega^2 L_0} - 2\frac{i}{\omega R_1}$. Apparently, there is $B_1 = B_2 = B_3$ at the fixed frequency f_0. Thus, the 2D circuit Laplacian can still be separated into two spins via the transformation of $J_2'(k) = T_2 J_2(k) {T_2}^{-1}$ at f_0. Taking spin down as an example, the corresponding circuit Laplacian at f_0 can be written in the form of

$$J_{2\downarrow}(\boldsymbol{k}) = \begin{pmatrix} B_1 & C_a + c_{12} & C_a + c_{13} \\ C_b + c_{12}^* & B_1 & c_{23} \\ C_b + c_{13}^* & c_{23}^* & B_1 \end{pmatrix}, \tag{S17}$$

where $C_a = i\left(\frac{1}{\omega_0 R_1} - C_0\right)$, $C_b = i\left(\frac{1}{\omega_0 R_1} + C_0\right)$, $c_{12} = -C_2 e^{-ik_x}$, $c_{13} = -C_2 e^{-i(k_x + \sqrt{3}k_y)/2}$ and $c_{23} = -C_2 e^{-i(-k_x + \sqrt{3}k_y)/2}$. Notably, the resistances with R_{1c} in m and n directions are also the critical parameter for the TCM to form a TDM for spin down. In addition, the TCM can also be delocalized to form a topological edge mode, which occupies all sites of the edge [9], as shown in spin down model of Figs. S7a and S7b. When we set all $R_1 = R_{1c}$ in n direction and keep all $R_1 = 0$ in m direction, the second-order corner mode is delocalized along the left edge, finally becoming an edge mode, while the TCM of spin up is more bound in n direction. Similarly, the TCM delocalized along the lower edge can be achieved by setting all $R_1 = R_{1c}$ in m direction and $R_1 = 0$ in n direction.

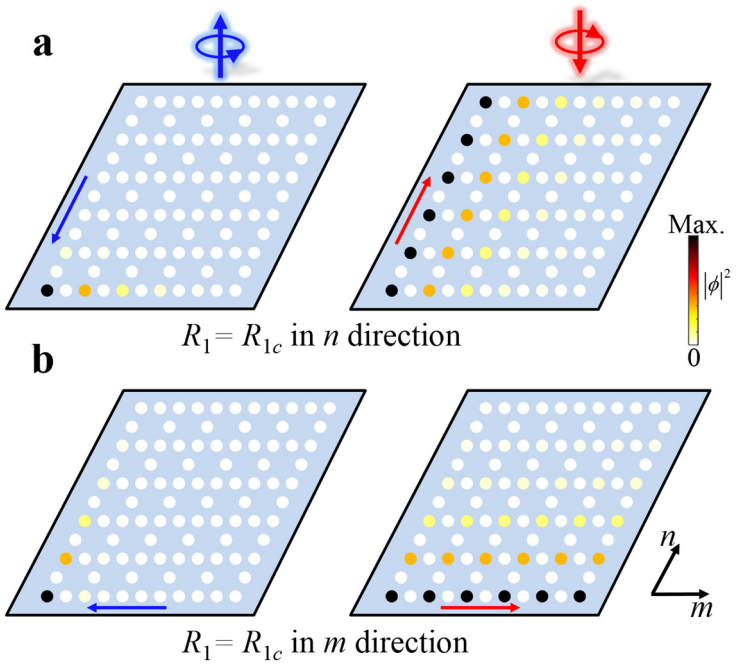

Figure S7 | The topological edge modes formed by TCMs. a, b Wavefunction intensity distributions of TCMs that are bound (spin up) and delocalized (spin down) in n and m directions, respectively. The total number of the circuit nodes is 192.

In addition to the delocalization of TCM shown in the main text, loss also makes the bulk modes and edge modes skin in corners of two spins, which so called corner NHSEs. Figures S8a and S8b display the numerical and experimental wavefunction distributions of bulk modes for spin up and spin down, respectively, which clearly exhibits the localization of bulk eigenstates at two corners. The bulk wavefunction $\bar{\phi}_B$ shown here is the average of all bulk eigenstates calculated by $\bar{\phi}_B = \frac{1}{N_B}\sum_i^{N_B}|\phi_i|^2$, where $N_B = 33$ is the number of bulk eigenstates for two spins. In addition, the numerical and experimental results of edge modes' corner NHSEs are shown in Figs. S8c and S8d, where the edge wavefunction $\bar{\phi}_E$ is calculated by $\bar{\phi}_E = \frac{1}{N_E}\sum_i^{N_E}|\phi_i|^2$ with $N_E = 6$. Excellent agreement between simulation and experiment demonstrates the ability of loss: it can not only delocalize the TBMs into bulk but also localize the bulk and edge modes into corners.

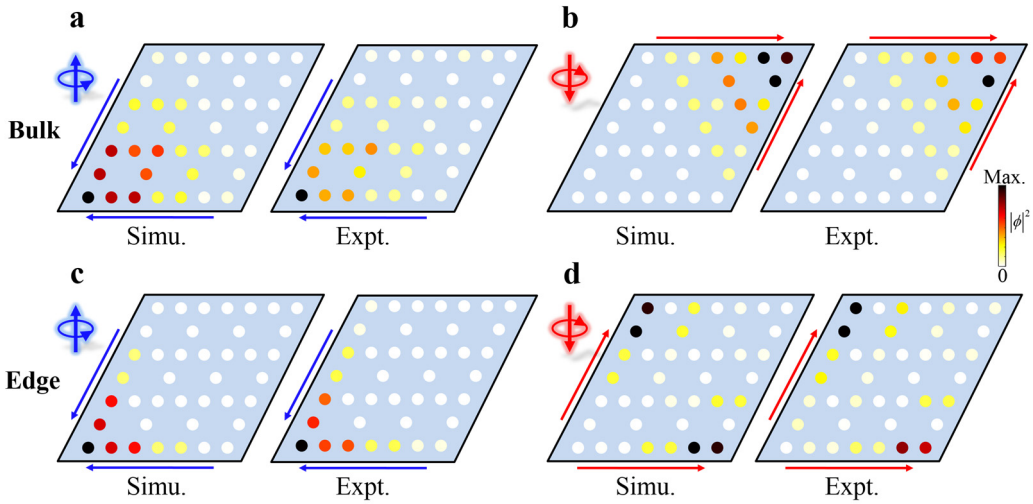

Figure S8 | Loss induced corner NHSEs of bulk and edge modes in a 2D electric circuit. a, b Average bulk wavefunction intensity distributions for spin up and spin down, respectively. **c, d** Average edge eigenstate intensity distributions for spin up and spin down, respectively. The circuit possesses a total of 80 nodes. The experimental frequency is $f = 174.8$ kHz.

7. Robustness of loss induced TDM to defects.

To demonstrate the loss induced TDM is still protected by topology, we provide corresponding results in the main text, showing the TDM persists with a broad frequency and against disorders in resistance with only minor deformations in the OBC spectra. Here, we numerically prove that loss induced TDM also robust against defects in a 2D passive electric circuit. When we remove a single node 1 near the lower-left corner of each layer and finally leave two defects, the lower-left TCM can still be delocalized to the top-right corner and forms an extended TDM for spin down, as shown in Fig. S9a. While the bound mode of spin up is not affected. In addition, when we remove a single node 2 of the circuit for each layer, as shown in Fig. S9b, neither TDM nor bound mode is affected.

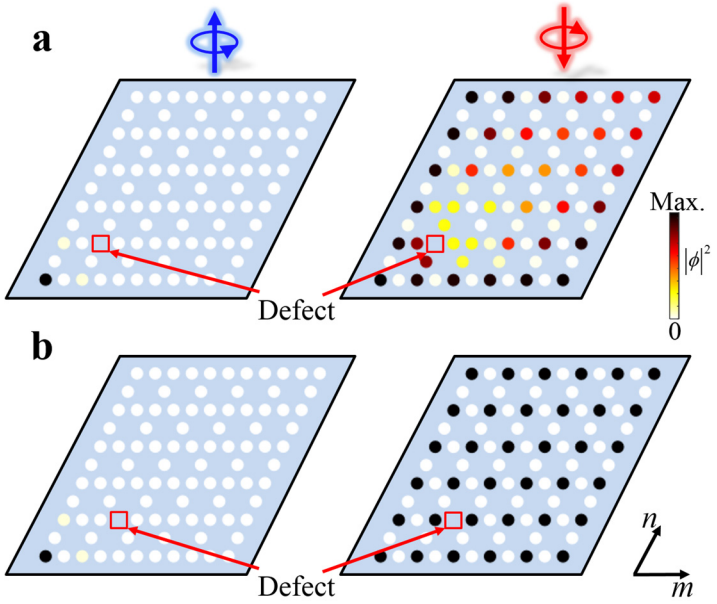

Figure S9 | Wavefunction intensity distributions after adding defects. a, b Wavefunction intensity distributions of bound mode (spin up) and TDM (spin down) with defects at node 1 and 2 near the lower-left corner, respectively. The total number of the circuit nodes is 190.

8. Details of 3D bilayer non-Hermitian lattice.

The Hamiltonian of the bilayer pyrochlore lattice shown in Fig. 5a of main text can be expressed as

$$H_2(\boldsymbol{k}) = \begin{pmatrix} 0 & i\gamma+h_{12} & i\gamma+h_{13} & i\gamma+h_{14} & 0 & -t_0 & -t_0 & -t_0 \\ i\gamma+h_{12}^* & 0 & h_{23} & h_{24} & t_0 & 0 & 0 & 0 \\ i\gamma+h_{13}^* & h_{23}^* & 0 & h_{34} & t_0 & 0 & 0 & 0 \\ i\gamma+h_{14}^* & h_{24}^* & h_{34}^* & 0 & t_0 & 0 & 0 & 0 \\ 0 & t_0 & t_0 & t_0 & 0 & i\gamma+h_{12} & i\gamma+h_{13} & i\gamma+h_{14} \\ -t_0 & 0 & 0 & 0 & i\gamma+h_{12}^* & 0 & h_{23} & h_{24} \\ -t_0 & 0 & 0 & 0 & i\gamma+h_{13}^* & h_{23}^* & 0 & h_{34} \\ -t_0 & 0 & 0 & 0 & i\gamma+h_{14}^* & h_{24}^* & h_{34}^* & 0 \end{pmatrix} \tag{S18}$$

where $h_{12} = t_1 e^{-i(k_x+k_y)/2}$, $h_{13} = t_1 e^{-i(k_y+k_z)/2}$, $h_{14} = t_1 e^{-i(k_x+k_z)/2}$, $h_{23} = t_1 e^{-i(k_z-k_x)/2}$, $h_{24} = t_1 e^{-i(k_z-k_y)/2}$ and $h_{34} = t_1 e^{-i(k_x-k_y)/2}$. Its basis is based on $\psi = [\psi_{1\mathrm{up}}, \psi_{2\mathrm{up}}, \psi_{3\mathrm{up}}, \psi_{4\mathrm{up}}, \psi_{1\mathrm{down}}, \psi_{2\mathrm{down}}, \psi_{3\mathrm{down}}, \psi_{4\mathrm{down}}]^T$. Similarly, it can

also be decoupled into into two spin parts with $H_3'(\boldsymbol{k}) = \begin{pmatrix} H_{3\uparrow}(\boldsymbol{k}) & 0 \\ 0 & H_{3\downarrow}(\boldsymbol{k}) \end{pmatrix}$ via the unitary transform $H_3'(\boldsymbol{k}) = T_3 H_3(\boldsymbol{k}) T_3^{-1}$, where the transform matrix can be expressed as

$$T_3 = \frac{1}{\sqrt{2}} I_4 \otimes \begin{pmatrix} 1 & i \\ 1 & -i \end{pmatrix}. \tag{S19}$$

The corresponding spin polarized eigenstates can be obviously obtained as $\psi_{\uparrow(\downarrow)} = \frac{1}{\sqrt{2}}[\psi_{1\text{up}} + (-)i\psi_{1\text{down}}, \psi_{2\text{up}} + (-)i\psi_{2\text{down}}, \psi_{3\text{up}} + (-)i\psi_{3\text{down}}, \psi_{4\text{up}} + (-)i\psi_{4\text{down}}]^T$.

The third-order corner modes can be characterized by the non-Hermitian bulk polarizations. In the 3D system, we can define the bulk polarization of the lowest band for 3D spin down model as $P_3 = \frac{1}{2\pi}\int_{b_3} dv_3$, where the Wannier band v_3 is calculated along the direction of the reciprocal lattice vector b_3 with (k_1, k_2) vary along (b_1, b_2) in momentum space [13], as shown in Fig. S10a. The bulk polarizations P_1 and P_2 in the other two directions can be obtained via the similar way. The corresponding topological phase diagram is shown in Fig. S10b, where the nontrivial phase with $P_3 = -1/4$ and trivial phase with $P_3 = 0$ indicate the Wannier centers located at the centers of the downward-pointing and upward-pointing tetrahedrons, respectively. It is also the same for spin up. The Wannier band v_3 for the critical parameters is shown in Fig. S10c.

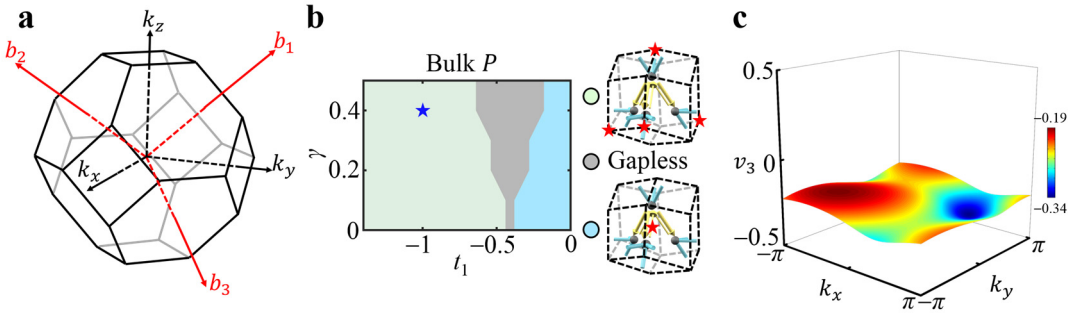

Figure S10 | Topological phases of the 3D spin down models. a First BZ of the pyrochlore lattice. **b** Topological phase diagram of 3D model with $t_0 = 0.6$. The red stars indicate the location of Wannier centers. The green, gray and blue colors indicate the nontrivial phase, gapless and trivial phase, respectively. **c** Wannier band v_3 varies

with k_x and k_y, whose intensity are indicated by colors. The red represents the maximum value, and blue represents the minimum value.

9. 3D passive electric circuit's design and property.

The 3D circuit Laplacian can be derived as $J_3(\boldsymbol{k}) = i\omega[H_3(\boldsymbol{k}) + E_3]$, where $H_3(\boldsymbol{k})$ is the same with Eq. (S18) through the correspondences. Each node of the 3D circuit is grounded through an inductance L_0 and a capacitance C_1. Meanwhile, nodes 2, 3 and 4 are all grounded two R_1 and four C_0; node 5 is grounded six C_0; nodes 6, 7 and 8 are all grounded two R_1 and two C_0. The diagonal matrix can be expressed as $E_3 = \mathrm{diag}(D_1, D_2, D_2, D_2, D_3, D_1, D_1, D_1)$, where $D_1 = 3C_0 + C_1 + 3C_2 - \frac{1}{\omega^2 L_0} - 3\frac{i}{\omega R_1}$, $D_2 = 4C_0 + C_1 + 3C_2 - 2\frac{1}{\omega^2 L_0} - 3\frac{i}{\omega R_1}$, $D_3 = 6C_0 + C_1 + 3C_2 - 4\frac{1}{\omega^2 L_0} - 3\frac{i}{\omega R_1}$. Obviously, there is $D_1 = D_2 = D_3$ at the fixed frequency f_0. Thus, the 3D circuit Laplacian can still be separated into two spins via the transformation of ${J_3}'(k) = T_3 J_3(k) {T_3}^{-1}$ at f_0. Taking spin down as an example, the corresponding circuit Laplacian at f_0 is expressed as

$$J_{2\downarrow}(\boldsymbol{k}) = \begin{pmatrix} D_1 & C_a + c_{12} & C_a + c_{13} & C_a + c_{14} \\ C_b + c_{12}^* & D_1 & c_{23} & c_{24} \\ C_b + c_{13}^* & c_{23}^* & D_1 & c_{34} \\ C_b + c_{14}^* & c_{24}^* & c_{34}^* & D_1 \end{pmatrix}, \tag{S20}$$

where $C_a = i\left(\frac{1}{\omega_0 R_1} - C_0\right)$, $C_b = i\left(\frac{1}{\omega_0 R_1} + C_0\right)$, $c_{12} = -C_2 e^{-i(k_x+k_y)/2}$, $c_{13} = -C_2 e^{-i(k_y+k_z)/2}$, $c_{14} = -C_2 e^{-i(k_x+k_z)/2}$, $c_{23} = -C_2 e^{-i(k_z-k_x)/2}$, $c_{24} = -C_2 e^{-i(k_z-k_y)/2}$ and $c_{34} = -C_2 e^{-i(k_x-k_y)/2}$. The resistances with R_{1c} in m, n and l directions are also the critical parameter for the TCM to form a TDM for spin down.

The intensity of the topological bound mode for spin up is experimentally measured in 3D, as shown in Fig. S11. The 3D spin lattice models are shown in Fig. S11a, the theoretical wavefunction intensity of third-order topological bound mode for spin up is shown in Fig. S11b. The measured OBC complex spectra and topological bound mode's wavefunction intensity are shown in Figs. S11c and S11d, respectively.

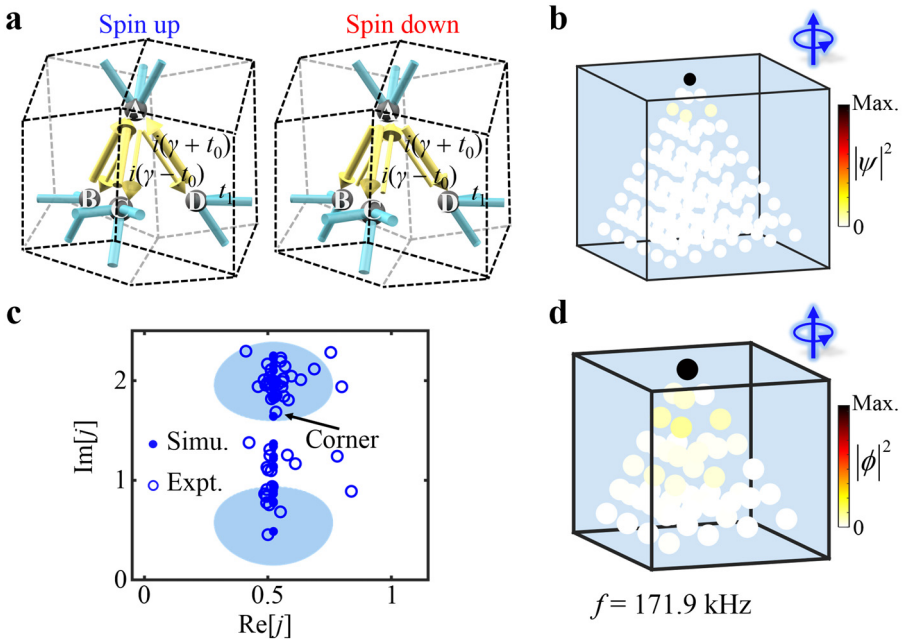

Figure S11 | Measured topological bound mode for spin up in 3D. a Schematic of spin lattice models. **b** Theoretical wavefunction intensity of third-order topological bound mode. **c** Simulated and measured OBC spectra. **d** Measured third-order topological bound mode. The experimental frequency is $f = 171.9$ kHz.

10. Effect of frequency variation on the topological properties of TBMs.

For the circuit with a given frequency $\omega = 2\pi f$, the Laplacian can be written as $J(\boldsymbol{k}) = i\omega[H(\boldsymbol{k}) + E]$, where the Hamiltonian has the same topological property with the Laplacian at any frequency. Therefore, we mainly focus on the circuit's Hamiltonian. Since the onsite part of each site is only equal at the critical frequency f_0 that satisfies equal positive and negative frequency hoppings, i.e., $\frac{1}{\omega_0^2 L_0} = C_0$, we only consider the influence of the frequency variation near the f_0 on the topological properties of the TBMs. At this time, the spin models can still be approximately obtained by the unitary transform of $J'(\boldsymbol{k}) = TJ(\boldsymbol{k})T^{-1}$.

For the spin down part of the 1D circuit, its topological invariants represented by the Bloch and non-Bloch winding numbers can also be calculated. The topological phase diagram of the 1D spin down model with frequency range 150-170 kHz is displayed in Fig. S12a. As observed, the topological property of the TBM characterized by the non-Bloch winding number will not be affected within a certain frequency range.

The localization property of the TBM characterized by the Bloch winding number will be influenced by the frequency change. When the frequency reaches f_0, it corresponds to a perfect TDM. The complex admittance spectra at the frequencies denoted by red and gray line in Fig. S12a are shown in Figs. S12b and S12c, respectively.

Furthermore, the non-Hermitian bulk polarizations are employed to describe the topological properties of the corner modes in 2D and 3D. The First BZs are shown in Fig. S12d. Similar to the calculated methods mentioned above, the bulk polarizations of 2D and 3D spin down models are shown in Figs. S12e and S12f, respectively. Notably, the corner modes maintain the nontrivial phase with $P_y = -1/2\sqrt{3}$ (2D) and $P_3 = -1/4$ (3D) unchanged within a certain frequency range.

In summary, within a certain frequency range, the topological properties of the 1D, 2D and 3D TBMs will not be affected by frequency variations even they become the TDMs. The Bloch winding number calculated in 1D illustrates that the frequency variation will affect the localization property of TBMs. However, the experimental results confirm that within a certain frequency range, the localization properties of the TDMs change very little, reflecting their broadband characteristics.

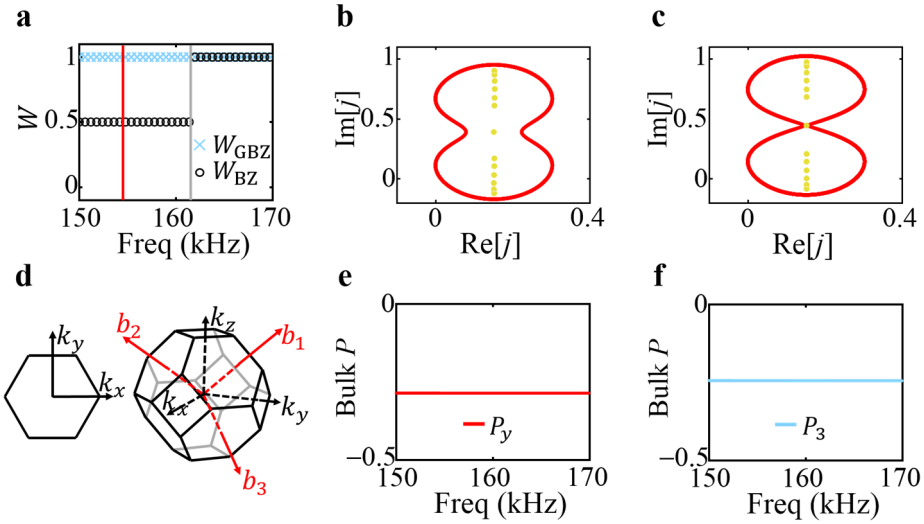

Figure S12 | Topological phases of 1D, 2D and 3D spin down models as a function of frequency. a Topological phase of 1D model. The red and gray lines mark 154 kHz and 161.8 kHz, respectively. **b**, **c** Complex admittance spectra of OBC and PBC at the marked frequencies of **a**, respectively. The red lines and yellow points represent the eigenvalues of PBC and OBC, respectively. **d** First BZs of the kagome and pyrochlore

models, respectively. **e**, **f** Topological phases of 2D and 3D models, respectively. All the element values of the circuit have been fixed except for the frequency.

11. Simulated realization of the loss induced acoustic TDM in 1D.

To be concrete, the 1D phononic crystal (PC) corresponding to the tight-binding model is constructed in Fig. S13a, where the acoustic cavity and coupling waveguide can be viewed as the site and hopping terms in the tight-binding model. The PC possesses 58 cavities and remains two topological end modes localized at the left end. All cavities are the same to ensure they possess the same eigenfrequencies f_E, which are designed as $f_E = 4314$ Hz. The lattice constant is $a = 65.1$ mm, the height and width of cavities are chosen as $h = 40$ mm and $b = 15$ mm, respectively. The intracell hopping is $t + i\gamma$ and the intercell one is t_1, where the designed loss is induced by the pink holes on waveguide, as shown in Fig. S13a. The impedance boundaries are set on the holes with an impedance of $Z = \rho_0 c_0$ to simulate the absorption of sound waves, where $\rho_0 = 1.29\ \mathrm{kg/m^3}$ and $c_0 = 345\ \mathrm{m/s}$ are the density and velocity of sound, respectively. The magnitude of the loss can be controlled by adjusting the area of holes. The positive and negative interlayer hoppings $\pm t_0$ can be achieved by using the dipole mode of cavity, as shown in Fig. S13b. Since the dipole modes in top and bottom cavities have the mirror symmetry for *x*-*y* plane, they have opposed phases for each other. When there is coupling waveguide among two cavities, the dipole mode splits into two modes with eigenfrequencies $f = f_E \pm \kappa_0$ [14]. For the positive hopping ($\kappa_0 > 0$), the frequency of the same phase mode is higher than that of opposed phase one, as shown in the top of Fig. S13b. On the contrary, there is a negative hopping ($\kappa_0 < 0$) shown in the bottom of Fig. S13b.

When we set the area of holes, the magnitude of loss is fixed. The critical parameters for forming the TDM correspond to the intersection points of the PBC and OBC bands, which can be identified by scanning the intercell hopping parameters while fixing the remaining parameters with $w = 5$ mm. Notably, we adjusted the hopping in PC by sweeping the side length w_1 of the waveguides, while keeping the waveguide lengths fixed at half the cavity length to ensure the center frequency remained

unaffected [15]. The corresponding numerical energy and eigenfrequency of tight-binding model and PC are shown in Figs. S13c and S13d, respectively, where the critical parameters are marked by the red stars with $w_1 = 8.5$ mm. As observed, although the PBC band is closed, the eigenfrequencies of TBMs are still in the gap of OBC band. The TBMs' eigenstates are subsequently simulated and the sound pressure fields are obtained within $3h/4$ of each cavity. The corresponding sound pressure fields of the spin polarized eigenstates can be obtained by the basis of $P_{\uparrow(\downarrow)} = \frac{1}{\sqrt{2}}[P_1 + (-)iP_3, P_2 + (-)iP_4]^T$. As shown in Fig. S13e, the full extended sound pressure distribution of spin down chain indicates the well-formed TDM, while the more bound pressure distribution of spin up chain represents the topological bound mode. The TBM in Hermitian case is displayed by black dotted line.

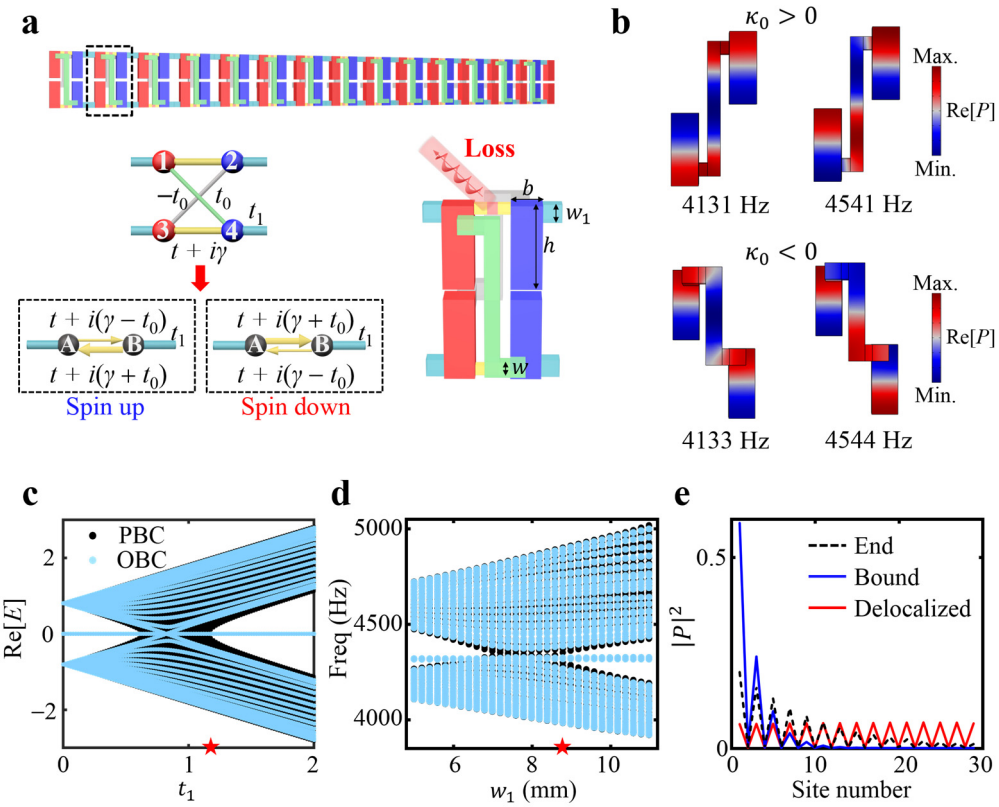

Figure S13 | Realization of the TDM in an 1D acoustic system. a Illustration of the 1D duplex PC lattice. Each unit cell consists of four sites 1-4 and can be decoupled into two independent spin models. The red and blue balls represent the corresponding sublattices. The yellow and light blue sticks are intracell and intercell hoppings, respectively. The red vortex represents loss. The grey and green sticks represent the

positive and negative hopping, respectively. These colors have the same meaning as those in the corresponding acoustic model. **b** Sound pressures of two eigenmodes generated by the positive and negative hoppings, respectively. **c**, **d** Energy and eigenfrequency bands of OBC as a function of t_1 and w_1, respectively. The parameters of tight-binding model are $t_0 = 0.6$, $t = 0.6$ and $\gamma = 0.4$. **e** Normalized sound pressure intensity distributions of TBMs. The TBM is fully delocalized for spin down and more localized for spin up.

12. Large-area single mode topological amplifier via loss induced TDM.

The time evolution of the field is expressed as $i\frac{\partial \boldsymbol{\psi}}{\partial t} = H\boldsymbol{\psi} - i\gamma_0\boldsymbol{\psi} + \frac{ig\boldsymbol{P}}{1+|\boldsymbol{\psi}|^2/I_{\mathrm{sat}}}$ [16], where H is the Hamiltonian of system, γ_0 is the global loss in each site, the third term indicates gain g via stimulated emission that is inherently saturable at I_{sat} and $\boldsymbol{P}$ represents the spatial profile of the pump. We begin with the 1D spin down model, setting $\gamma_0 = 0.01$ on all sites, $g = 0.016$ on all A sites and $I_{\mathrm{sat}} = 10$. The equivalent non-reciprocal imaginary hopping is constructed by loss γ. As shown in Fig. S14a, sufficient gain causes the imaginary part of the TBM's energy to become positive, driving it to become the single amplification mode, whereas bulk modes maintain negative energies. The instantaneous total intensity of the amplification mode with $I_t(t) = \sum_{i=1}^{N}|\psi_i(t)|^2$ can be derived by solving the time evolution of the field. The initial field of $\boldsymbol{\psi}$ is set with random complex amplitudes of $0.005(m + ni)$ and $m, n \in (-1,1)$, while the Hamiltonian is set with $\gamma = 0$ for TBM and $\gamma = \gamma_c$ for TDM. The numerical results are shown in Fig. S14b, indicating that the amplification modes of TBM and TDM finally become steady after experience a certain period of evolution, respectively. As observed, even under the same gain conditions, the total field intensity of TDM is much larger than that of TBM, displaying the high energy conversion. Meanwhile, the corresponding intensity distributions of the wavefunction evolving over time are shown in Figs. S14c and S14d, respectively. These results demonstrate that the TDM induced by loss can indeed be employed to realize energy amplification across the whole lattice.

Compared with amplifier constructed by localized TBM, which can only amplify energy at specific sites and often require huge bulk lattices, the amplification mode constructed by TDM can amplify energy at all sites, regardless of the lattice size. This significantly improves the spatial utilization and flexibility of the amplifier, as multi-channel energy output can be achieved with only a small lattice, greatly saving costs and footprints. The uniform intensity distribution of TDM is also beneficial to avoiding excessive energy concentration at a single point, thereby preventing device damage. Meanwhile, it is demonstrated that by employing the simple design with the loss and combining the gain, such an extended amplification mode with nontrivial topological property can be achieved. Compared with the complex non-reciprocal regulation, this approach is undoubtedly conducive to the development of amplifier devices and promotes the exploration and development of applications based on topological insulators with delocalized modes.

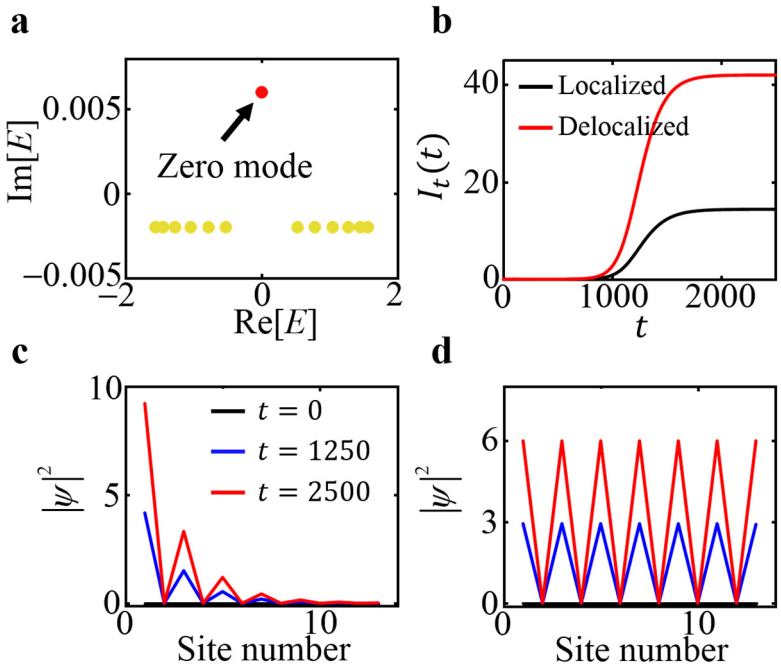

Figure S14 | Large-area single mode topological amplifier achieved by loss induced TDMs in 1D case. a Complex spectrum of OBC for spin down model with site number of $N = 13$. The zero mode with positive imaginary energy is exactly the single amplification mode. **b** Time evolution of the instantaneous total intensity $I_t(t)$ for TBM and TDM with $\gamma = 0$ and $\gamma = \gamma_c$, respectively. **c**, **d** Wavefunction intensities

of the TBM and TDM at different times, respectively.

13. Discussion of the uncertainties in experimental measurements.

The uncertainties in experimental measurements here are mainly originated from three aspects.

The first is the inevitable nominal errors between circuit components and their true values. The circuit components with manufacturing tolerances here are $C_0 = 220$ nF $(\pm 5\%)$, $C_1 = 68$ nF $(\pm 5\%)$, $C_2 = 369$ nF $(\pm 5\%)$, $L_0 = 4.4$ uH $(\pm 10\%)$ and $R_1 = 6.65\ \Omega\ (\pm 0.1\%)$, which cause the actual circuit Laplacian to deviate from the theoretical one. The fluctuating component values cause the measured eigenvalue spectra to fluctuate accordingly, while the corresponding wavefunction distribution of the TDM is no longer uniformly extended. As a demonstration, we introduce the nominal error of each component into the numerical calculation as the disorder and calculate 30 times. The spectra under OBC in 2D are presented in Figs. S15a and S15b for two spins. The corner modes' wavefunctions from a randomly selected single calculation is shown on the right side. These calculated results are similar to the fluctuated experimental results, which demonstrate our point.

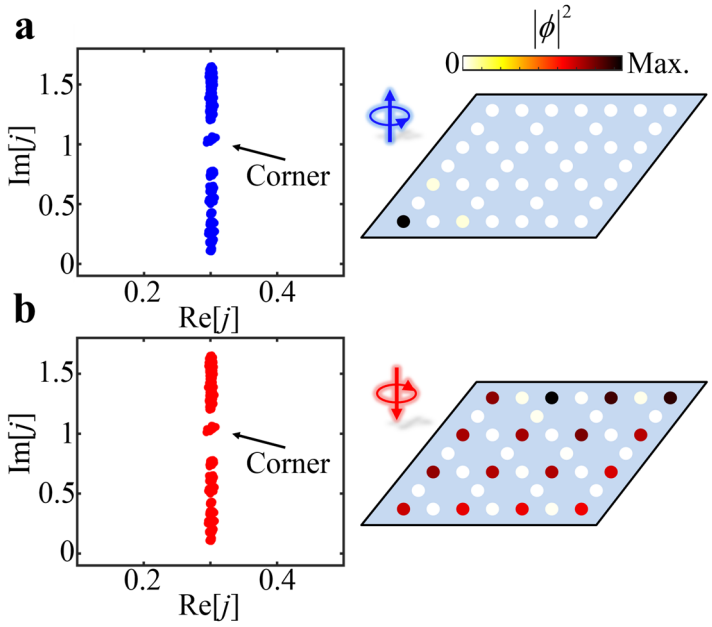

Figure S15 | Calculated results that consider the manufacturing tolerances of circuit components. a, b Calculated OBC spectra at critical frequency under disorders

for two spins, respectively. Each spectrum is calculated 30 times. The corresponding wavefunction intensities of the corner modes for a randomly selected calculation are shown on the right. The blue and red indicate spin up and spin down, respectively.

In addition, the deviations of components' central values from their nominal values cause a corresponding shift in the critical frequency, which results in a discrepancy between the measured frequency of the TDM and its theoretical value. As a simple example, we assume that the average value of the inductances for interlayer hopping decreases by 8% compared to the previous value. The OBC imaginary spectrum of spin down in a certain frequency range is shown in Fig. S16a. In this case, the critical frequency is no longer $f_0 = 161.8$ kHz but becomes $f_0' = 168.8$ kHz, and the corner mode's wavefunction at 161.8 kHz is no longer distributed very uniformly compared with it at 168.8 kHz, as shown in Figs. S16b and S16c.

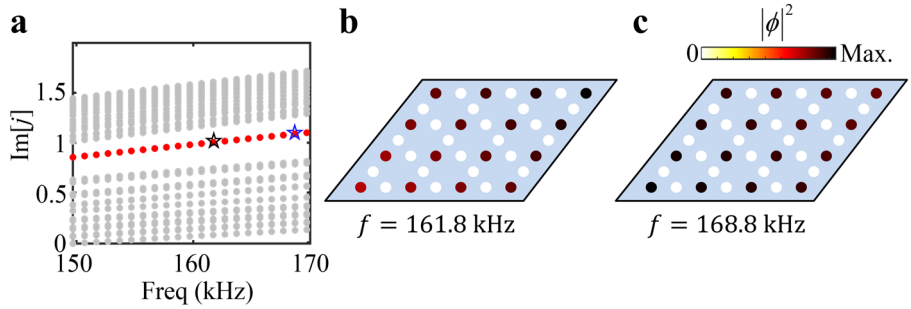

Figure S16 | Frequency changes induced by variations in the central values of circuit components. a Calculated OBC imaginary spectra in a certain frequency range for spin down. **b, c** Wavefunction intensities of the corner mode at frequencies marked by black and blue stars in a, respectively. Owing to the deviation of circuit component values from their central values, the wavefunctions deviate from the ideal TDM.

The third is the uncertainty introduced by experimental instrument and the circuit PCB itself. Experimental instruments introduce noise (or preserve noise during signal acquisition). This noise is superimposed on the useful voltage signal, resulting in a finite signal-to-noise ratio (SNR) in the measured responses and causing them to exhibit fluctuations. For nodes with inherently small voltage responses, the noise introduces a

higher relative error in the measurements. To mitigate such errors, it is common practice to increase the amplitude of the input signal and implement proper grounding between the instrument and the PCB circuit. Due to the integrated design of the PCB, there is mutual interference between components, as well as between wires during the circuit's response. For example, inductors in the PCB exhibit mutual inductance with other inductors, which affects their respective values; meanwhile, there are interactions between parallel wires, the wires need to be disorganized to avoid parallel interference between them [10].

Therefore, experimental measurement uncertainty can be minimized by selecting high-accuracy components, employing precision instruments, improving the signal-to-noise ratio (SNR), and optimizing PCB layout to mitigate parasitic effects and crosstalk.

Supplementary references

1. Yao, S. Y.&Wang, Z. Edge States and Topological Invariants of Non-Hermitian Systems. *Phys. Rev. Lett.* **121,** 086803 (2018).
2. Zhang, K., Yang, Z. S.&Fang, C. Universal non-Hermitian skin effect in two and higher dimensions. *Nat. Commun.* **13**, 2496 (2022).
3. Yin, C. H., Jiang, H., Li, L. H., Lü, R.&Chen, S. Geometrical meaning of winding number and its characterization of topological phases in one-dimensional chiral non-Hermitian systems. *Phys. Rev. A* **97**, 052115 (2018).
4. Zhu, W. W., Teo, W. X., Li, L. H.&Gong, J. B. Delocalization of topological edge states. *Phys. Rev. B* **103**, 195414 (2021).
5. Aquino, R., Lopes, N.&Barci, D. G. Critical and noncritical non-Hermitian topological phase transitions in one-dimensional chains. *Phys. Rev. B* **107**, 035424 (2023).
6. Lee, C. H.&Thomale, R. Anatomy of skin modes and topology in non-Hermitian systems. *Phys. Rev. B* **99**, 201103(R) (2019).
7. Verma, S.&Park, M. J. Non-Bloch band theory of subsymmetry-protected topological phases. *Phys. Rev. B* **110**, 035424 (2024).
8. Zhong, J. E., Wang, H. M.&Fan, S. H. Pole and zero edge state invariant for one-dimensional non-Hermitian sublattice symmetry. *Phys. Rev. B* **110**, 214113 (2024).
9. Wang, W., Wang, X. L.&Ma, G. C. Non-Hermitian morphing of topological modes. *Nature* **608,** 50-55 (2022).
10. Zou, D. Y. et al. Observation of hybrid higher-order skin-topological effect in non-Hermitian topolectrical circuits. *Nat. Commun.* **12**, 7201 (2021).
11. Helbig, T. et al. Generalized bulk-boundary correspondence in non-Hermitian topolectrical circuits. *Nat. Phys.* **16**, 747-750 (2020).
12. Yao, S. Y., Song, F.&Wang, Z. Non-Hermitian Chern Bands. *Phys. Rev. Lett.* **121**, 136802 (2018).
13. Weiner, M., Ni, X., Li, M. Y., Alù, A.&Khanikaev, A. B. Demonstration of a third-order hierarchy of topological states in a three-dimensional acoustic metamaterial. *Sci. Adv.* **6**, eaay4166 (2020).
14. Qi, Y. J. et al. Acoustic Realization of Quadrupole Topological Insulators. *Phys. Rev. Lett.* **124**, 206601 (2020).
15. Chen, Z. G., Wang, L. C., Zhang, G. Q.&Ma, G. C. Chiral Symmetry Breaking of Tight-Binding Models in Coupled Acoustic-Cavity Systems. *Phys. Rev. Appl.* **14**, 024023 (2020).
16. Harari, G. et al. Topological insulator laser: Theory. *Science* **359**, eaar4003 (2018).